Article:

Smith, CJ, Forster, PM and Crook, R (2016) An all-sky radiative transfer method to predict optimal tilt and azimuth angle of a solar collector. Solar Energy, 123. 88 - 101. ISSN 0038-092X

https://doi.org/10.1016/j.solener.2015.11.013

An all-sky radiative transfer method to predict optimal tilt and azimuth angle of a solar collector

Christopher J. Smith[a,*], Piers M. Forster[b], Rolf Crook[a]

[a] *Energy Research Institute, School of Chemical and Process Engineering, University of Leeds, Leeds LS2 9JT, United Kingdom*

[b] *Institute for Climate and Atmospheric Science, School of Earth and Environment, University of Leeds, LS2 9JT, United Kingdom*

Abstract

This paper describes a radiative transfer method for calculating radiances in all-sky conditions and performing an integration over the view hemisphere of an arbitrary plane to calculate tilted irradiance. The advantage of this method is the combination of cloud parameters inside the radiative transfer model with a tilt procedure. For selected locations this method is applied with cloud, ozone, water vapour and aerosol input data to determine tilted irradiance, horizontal irradiance and optimal tilt angle. A validation is performed for horizontal and tilted irradiance against high-quality pyranometer data. For 27 sites around the world, the annual horizontal irradiation predicted by our model had a mean bias difference of +0.56% and a root-mean-squared difference of 6.69% compared to ground measurements. The difference between the annual irradiation estimates from our model and the measurements from one site that provides tilted irradiance were within ±6% for all orientations except the north-facing vertical plane. For European and African sites included in the validation, the optimal tilt from our model is typically a few degrees steeper than predictions from the popular PVGIS online tool. Our model is generally applicable to any location on the earth's surface as the satellite cloud and atmosphere data and aerosol climatology data are available globally. Furthermore, all of the input data are standard variables in climate models and so this method can be used to predict tilted irradiance in future climate

*Corresponding author. Tel: +44 (0)113 343 2498
Email address: pmcjs@leeds.ac.uk (Christopher J. Smith)

experiments.

Keywords: radiative transfer, tilt, radiance, cloud

1. Introduction

The orientation of a plane solar collector such as a PV panel can be varied in the tilt and azimuth directions in order to maximise the incident irradiance. One way to accurately assess the solar resource available on a tilted plane and determine the optimum angle to orient a fixed angle PV panel in the real world, is to position pyranometers in several plane orientations and record the sum of irradiance over a sufficiently long period of time. In practice this is rarely completed, so models to predict the tilted irradiance are used.

There are two concepts fundamental to the method described. Firstly, cloud optical properties, from satellite retrievals, are integrated into the radiative transfer (RT) calculation. Secondly, tilted irradiance is derived from a surface radiance field. RT methods are frequently used to model clear-sky solar irradiance (Bird and Riordan, 1986; Gueymard, 1995; Mueller et al., 2004). Sometimes cloud effects are introduced as an adjustment to the clear-sky values depending on satellite-derived cloud albedo (Cano et al., 1986) or tuned based on observed historical ground-level irradiance (Nann and Emery, 1992). In other studies cloud effects are included directly. Lohmann et al. (2006) used data from meteorological reanalyses and cloud parameters from the International Satellite Cloud Climatology Project (ISCCP) with a two-stream radiative transfer code to estimate surface irradiance. Deneke et al. (2008) used cloud retrievals from Meteosat in combination with RT simulations to estimate solar irradiance in the Netherlands. Mueller et al. (2009) used a lookup table approach for clouds with transmissions pre-calculated with RT and values interpolated from the lookup table. They used a cloud effective radius of 10 μm for water droplets using the Hu and Stamnes (1993) parametrisation of the phase function and did not consider ice clouds. While this may be sufficient for horizontal fluxes, this approach is less accurate when calculating the radiances required for the tilted irradiance. Behrendt et al. (2013) used the SOLIS clear-sky model with cloud adjustment to determine the spectral effects on different PV technologies. A separate run with clouds specified directly inside the radiative transfer model was performed. The difference in spectral transmission between SOLIS and the RT solution using the libRadtran package (Mayer and Kylling, 2005) is about 5% in average photon energy for thick cloud cover (optical depth of 60) at a solar zenith angle of 60°. More recently, the UniSky simulator software (Kocifaj and Fečko, 2014; Kocifaj, 2015) includes the effects of a 3D cloud field to model ground-level radiances. Current satellite products often include the required cloud optical properties, namely cloud phase (water or ice), cloud optical depth, and cloud droplet effective radius, to allow RT simulations including clouds to be performed. One motivation for inclusion of clouds inside the RT calculation is for the development of solar energy models that can be applied to a wide variety of historical, current and future datasets, for example meteorological reanalyses or climate models, as well as satellite observations. Another is the spectral effects of cloud attenuation are better captured with RT simulation, which is important for PV.

After the directional radiances have been calculated from the RT simulation, integrating the radiance field over the direction of interest will provide the tilted irradiance. McArthur and Hay (1981) used radiance distributions obtained from fish-eye photographs and obtained agreement to ±10% for horizontal diffuse irradiance and ±5% for tilted irradiance on a south-facing plane, in a variety of sky conditions. Brunger and Hooper (1993) derived an empirical model for the sky radiance distribution calculated from observations of clearness index (ratio of surface irradiance to extraterrestrial irradiance) and zenith angle. Similarly Gueymard (1987) derived the sky radiance distribution by producing different anisotropic sky radiance distributions for a clear-sky and an overcast sky. The all-sky radiance distribution was calculated as a weighted sum of the clear and overcast cases with cloud transmission as the weighting factor.

Other popular anisotropic tilted irradiance models (e.g. Bugler (1977); Klucher (1979); Willmott (1982); Hay and Davies (1980); Skartveit and Olseth (1986); Reindl et al. (1990); Perez et al. (1990); Muneer (1990)) are varyingly complex functions of the horizontal diffuse and direct irradiance measurements along with solar position and panel orientation. A comparison between ten tilt models at the NREL site at Golden, Colorado, USA, found that most anisotropic models did not predict irradiance with a satisfactorily low error for tilted planes compared to the bounds of instrumental error from pyranometers (Gueymard, 2009). An intercomparison of 15 models (4 isotropic and 11 anisotropic) in Denmark, France and Spain again found that no one anisotropic model generally performed better than the others consistently when considering different cloud conditions, tilt angles and azimuth angles (Gracia-Amillo and Huld, 2013). Therefore, the continued development of tilt models for all-sky conditions is desirable.

In this paper, the optimal tilt angle of a fixed-angle solar collector is considered. For comparison with the PVGIS method, the panel is oriented towards the equator, although it is also possible to optimise azimuth as shown in section 4.3. In the absence of horizon obstruction, shading, or radically different morning and afternoon weather conditions, the equatorial direction provides the best azimuthal alignment. The tilt angle of integration is varied to find the irradiance at each angle and summed over a year of operation to determine the optimal tilt. The model is tested against the tilted irradiance model in PVGIS and compared to tilted irradiance measurements from NREL.

2. Determining tilted irradiance from radiances

The irradiance on a tilted plane angled at tilt β and azimuth γ is a combination of the downwards and upwards radiance fields such that the bounds of the integration is over the hemisphere with base in the plane of the solar collector (Gueymard, 1987):

$$I_T = \int_0^{2\pi} \int_0^{\theta_m} L(\theta, \phi) \cos\theta_d \sin\theta \, \mathrm{d}\theta \, \mathrm{d}\phi \tag{1}$$

where the angle between the normal of the tilted plane and the radiance direction of interest is given by

$$\cos\theta_d = \cos\beta\cos\theta + \sin\beta\sin\theta\cos(\phi - \gamma) \tag{2}$$

and the bound of the integration θ_m is in the plane of the solar collector such that

$$\theta_m = \frac{\pi}{2} - \tan^{-1}(\cos(\phi - \gamma)\tan\beta). \tag{3}$$

The radiance field L is calculated at a resolution of 3° in the polar direction and 10° in the azimuthal direction using the `DISORT` radiative transfer code (Stamnes et al., 2000), as part of the libRadtran package (Mayer and Kylling, 2005), with a pseudo-spherical correction to improve accuracy at low solar elevations (Dahlback and Stamnes, 1991). θ is the polar angle and ϕ is the azimuthal angle. The radiative transfer equation is solved numerically with 16 streams, the minimum recommended for calculating radiances (Mayer et al., 2012). Eq. (1) is approximated numerically by summing each radiance element over small solid angles $\Delta\theta\Delta\phi$ such that

$$I_T \approx \sum_j \sum_k L(\theta_j, \phi_k) W \Delta\theta_j \Delta\phi_k \tag{4}$$

where $W = \max(0, \cos\theta_{dj} \sin\theta_j)$ to ensure only the radiances in the field of view of the solar collector are counted (McArthur and Hay, 1981). At non-zero tilts, the field of view will include some upwelling radiances from the ground which depend on the surface albedo and exclude any sky radiances emanating from directions behind the solar collector. $\cos\theta_{dj}$ is as given in eq. (2) with (θ, ϕ) replaced with (θ_j, ϕ_k).

To perform a complete calculation line-by-line over the whole solar spectrum for 61×36 radiance directions is infeasible in terms of computational time, so the correlated-k method (Kato et al., 1999) is used to divide the solar spectrum into 32 wavelength bands with similar atmospheric absorption properties. The calculation in eq. (4) is performed for each correlated-k band and the broadband radiance for each (θ_j, ϕ_k) pair is obtained by summing up I_T for each of the 32 correlated-k bands.

The numerical approximation in eq. (4) is performed for the diffuse irradiance only. The direct normal irradiance (DNI) is simpler to calculate. From the Beer-Lambert law the DNI is

$$I_B = I_0 \exp(-m\tau) \tag{5}$$

where I_0 is extraterrestrial irradiance and m is air mass. The optical depth τ describes the likelihood that a ray travels to the surface of the earth without being absorbed or scattered.

τ is the overall sum of the optical depths of all extinction phenomena in the atmosphere, e.g. mixed gases, ozone, water vapour, aerosols and cloud droplets. For a tilted plane, the direct incident irradiance is

$$I_{BT} = I_B \cos\theta_i \tag{6}$$

where the incident angle θ_i follows a similar form to eq. (2):

$$\cos\theta_i = \cos\beta\cos\theta_z + \sin\beta\sin\theta_z\cos(\phi_a - \gamma). \tag{7}$$

Here, θ_z is the solar zenith angle and ϕ_a is the solar azimuth angle.

The radiative transfer method bears another advantage over empirical tilt models in that no assumption of the size and shape of the circumsolar region is made. When making ground irradiance measurements, the direct irradiance is not usually discernible from diffuse sky irradiance that has been scattered into the region of the solar disc or diffuse radiation emanating from the solar region that has been caused by strongly forward scattering aerosol or thin cloud. This can cause issues in calculating the direct and diffuse contributions as a decision has to be made on the angular size of the circumsolar region (Blanc et al., 2014). Often a half-angle of 2.5° is used with all irradiance inside this region treated as direct. In our model, all scattered radiation is treated as diffuse regardless of the scattering direction with the directional distribution handled by the radiance field.

3. Inputs into the model

To generate the radiance field, inputs of the atmospheric state, location altitude, clouds, aerosols and surface albedo are required. Although any climate, satellite or reanalysis dataset that provides all of the necessary inputs can be used, we use the Moderate Resolution Imaging Spectroradiometer (MODIS) instrument data on the Aqua and Terra satellites for all parameters except aerosols for which we use a climatological run from a dedicated aerosol model (GLOMAP). The Terra satellite overpasses the equator at approximately 10:30 local solar time daily and the Aqua satellite overpasses at approximately 13:30 daily. Therefore, synoptic diurnal differences between the morning and afternoon can be partially captured. MODIS Level 3, 8-day mean data for ozone, water vapour, and cloud parameters (MOD08E3 and MYD08E3 data series, both Collection 5.1) were used. Surface albedo was obtained from the combined Terra and Aqua 16-day running mean albedo product MCD43C3, which is updated every 8 days. The resolution of the atmosphere and cloud data is $1^\circ \times 1^\circ$ and the albedo data is $0.05^\circ \times 0.05^\circ$. All data is freely available from the MODIS portal at `http://modis-atmos.gsfc.nasa.gov/`. 8-day time resolution is used as a trade-off between capturing fluctuations in weather conditions and computational efficiency. Daily and monthly timesteps are also available for the Level 3 MODIS data.

3.1. Atmosphere

Well-mixed gases in the atmosphere are a source of Rayleigh scattering which is dependent on wavelength. Shorter wavelengths are scattered more strongly according to the well-known λ^{-4} relationship.

libRadtran contains the set of six standard AFGL atmospheres (Anderson et al., 1986) which are tropical, mid-latitude summer and winter, sub-Arctic summer and winter, and US standard. The location and time of year dictates which particular atmosphere was selected in the calculation, however the impact of mixed gases on the final result is negligible (Oumbe et al., 2008; Mueller et al., 2009). Ozone is a strong absorber in the ultraviolet range and water vapour has absorption bands located throughout the near infrared, so the total atmospheric column depth of ozone and water vapour are taken from the MODIS data.

3.2. Clouds

Clouds are both the largest attenuating factor in the transmission of solar radiation and the source of the largest uncertainty for many regions of the world, the principal exceptions being in areas of high aerosol optical depth and infrequent clouds such as deserts. Both liquid and ice water clouds exhibit complex scattering properties. The radiative properties of clouds are determined by cloud droplet effective radius r_{eff}, single scattering albedo ω, phase function $P(\mu)$ where μ is the cosine of the scattering angle, and the cloud water content C which is the mass of cloud droplets present in a given volume. The cloud optical depth τ_c is a function of C and r_{eff}. The single scattering albedo determines the probability that if a ray collides with a cloud droplet, it is scattered rather than absorbed. The phase function describes the directional distribution of scattering event and hence is important in determining the final diffuse irradiance field.

For calculating radiances it is recommended to use the full Mie scattering parametrisation for liquid cloud droplets (Mayer et al., 2012) which provide ω and $P(\mu)$ as a function of wavelength. This is available as an extension to the core libRadtran package in the form of pre-calculated lookup tables generated using the Wiscombe (1980) Mie scattering code.

Ice clouds pose a particular complexity as ice crystals form in a variety of habits (shapes), on which the scattering phase function is strongly dependent. Additional morphological features such as surface roughness and trapped air bubbles also affect the phase function (Xie et al., 2006, 2012). The cloud retrieval algorithm for Collection 5.1 in MODIS uses a mixture of particle habits depending on the maximum diameter D_{max} of the ice crystals: 50% solid columns, 15% 3D bullet rosettes and 35% hexagonal plates for particles where $60 < D_{\text{max}} < 1000$ μm, and 45% solid columns, 45% hollow columns and 10% aggregates for particles where $1000 < D_{\text{max}} < 2000$ μm (Baum et al., 2005; Menzel et al., 2010; Minnis et al., 2011). A definition of 100% solid columns has been used in our model due to the difficulties of mixing habit types and the fact that solid columns make up the largest part of the mixture in the range of $60 < D_{\text{max}} < 2000$ μm corresponding to r_{eff} of approximately 20–120 μm, encompassing the majority of ice cloud effective radius retrievals. Out of the single-habit assumptions, solid columns provide the best estimates of ice water content and r_{eff} (Baum et al., 2005). The ice scattering has been represented by a double Henyey-Greenstein (DHG) phase function using the Key et al. (2002) model. The DHG is a convenient simplification of the real phase function that is suitable for modelling radiances due to its ability to somewhat account for the forward and backward scattering peaks better than the simpler single Henyey-Greenstein (HG) phase function (Mayer et al., 2012). In order to correctly model ice cloud scattering a full phase matrix scattering code should be used (e.g. Baum et al. (2014)), however the number of Legendre coefficients that need to be calculated for each scattering phase function make its use computationally prohibitive for multiple calculations. The DHG phase function is smooth and does not include effects such as the 22° and 46° halo scattering peaks present in pristine hexagonal columns and plates. The roughened hexagonal column phase function has a less strong forward scattering component than pristine hexagonal columns and does not exhibit a halo effect, therefore is represented better by the DHG phase function. The assumption of roughened hexagonal columns provides the lowest RMS error in optical depth for MODIS retrievals (Xie et al., 2012) adding justification for the smooth DHG phase function approximation.

Owing to the large uncertainties in modelling clouds in time and space, it was decided to use a simplified approach with two atmospheric columns, one clear and the other overcast. The resulting radiance distribution is weighted between the two situations based on cloud fraction c_f. To define the cloudy column, the cloud liquid water content C_w, cloud ice water content C_i (both g m^{-3}), cloud fraction c_f, cloud height h, and r_{eff} are used. r_{eff} may be, and usually is, different for liquid and ice droplets. Where both liquid and ice clouds are present, they are aggregated into the same column to create one mixed-phase cloud. The cloud is defined as having a vertical depth of 1 km except where the cloud top height is less than 1 km above the ground in which case it extends down to the surface. For single scattering albedos $\omega \to 1$, which is the case for the majority of solar wavelengths (Hu and Stamnes, 1993), the fraction of transmitted to incident irradiance is approximately independent of the cloud geometric height. This has previously been demonstrated in RT calculations (Rozwadowska, 2004; Oumbe et al., 2008). For mathematical convenience and consistency with other investigations (e.g. Lohmann et al. (2006)) the somewhat arbitrary depth of 1 km has been chosen. C_w, C_i, c_f and r_{eff} are all available from the MODIS data. Currently h is only reported for Aqua, so cloud top pressure, which is available from both satellites, was converted to height for both Terra and Aqua data using the hydrostatic equation.

3.3. Aerosols

A monthly aerosol climatology is provided by the GLOMAP model (Scott et al., 2014) at a resolution of $2.8^{\circ} \times 2.8^{\circ}$, which specifies ω, the asymmetry parameter g, and aerosol optical depth τ_a for 6 wavelength bands in the shortwave spectrum on 31 pressure levels. g describes the mean cosine of the scattering angle from $P(\mu)$ and ranges from -1 for backscattering to $+1$ for forward scattering. The species included are sulphate, sea-salt, black carbon and particulate organic matter aerosols in four size modes. A HG phase function is specified in our model, which has the large computational advantage of completely parametrising the phase function by g. MODIS data for aerosol has not been used as aerosol properties are not always available over land, particularly in desert regions which are important for solar energy and aerosols are prevalent.

3.4. Albedo

The surface albedo is the proportion of downwards irradiance that is reflected by the earth's surface. In reality, surface albedo is a function of wavelength and solar zenith angle as direct and diffuse irradiance components have different reflectance properties. Albedo is important in the tilted irradiance calculation as it defines the amount of reflected irradiance available from the ground that is available to a solar collector. Even at zero tilts, a higher surface albedo can increase downwards irradiance due to multiple reflections between surface and atmosphere, particularly if clouds are present (Gueymard, 2009).

The black-sky and white-sky albedos are calculated from the bi-directional reflectance distribution function (BRDF). Black-sky albedo is the albedo assuming all direct irradiance and no diffuse irradiance and is a function of solar zenith angle, whereas white sky albedo assumes a purely diffuse isotropic source and is independent of solar geometry. We have used the white sky albedo in this simulation due to the solar zenith independence. Deneke et al. (2008) has shown that this does not introduce significant error even in thin clouds. Surface albedo is spatially and temporally variable, even throughout the course of the same day (Gueymard, 2009), with the surface properties within a few metres of the solar collector of greatest importance.

4. Application of the model

One year of atmosphere, cloud and albedo data from 2013 was input into the model, and the solar zenith and azimuth were calculated at the centre of each hour for the middle day in each 8 day period. The diffuse radiance field L and direct normal irradiance I_B for each hour are the outputs from libRadtran. Plane irradiance for a particular tilt and azimuth is obtained by applications of eqs. (4) and (6) and adding together the results.

4.1. Radiance distributions

Fig. 1 shows the diffuse radiance distributions for clear sky, overcast sky and all sky (combination of clear and overcast), for a typical midday hour in northern European summer. The clear-sky case includes mixed gas, water vapour, ozone and aerosol attenuation. The anisotropy of clear-sky diffuse radiation due to the circumsolar region, and to a lesser extent the bright section near the horizon, can be seen from fig. 1(a). If an overcast sky is assumed (fig. 1(b)), it can be seen that the radiance distribution is much different, with a maximum intensity between the solar position and zenith which becomes apparently uniformly less intense away from this maximum towards the horizon. Fig. 1(c) shows the all-sky weighted radiance distribution taking into account the cloud fraction, which for this hour was 56.4%. The circumsolar peak is still apparent, but the horizon brightening contribution is hard to discern and the remaining sky radiance is more isotropically distributed than in the clear-sky case.

4.2. Tilted irradiance map

The radiance distributions for the same location were integrated over all polar and azimuthal alignments using eq. (4), and the direct beam included, to provide a tilted irradiance map (fig. 2). Fig. 2(a) shows that when there are no clouds, the ideal panel alignment is more or less normal to the solar beam. There is a fairly wide tolerance around the optimal position as a result of the cosine of incidence angle being approximately 1 for small incidence angles. Fig. 2(b) shows that in an overcast sky, the ideal panel alignment is horizontal and independent of the solar direction even though the corresponding radiance distribution is

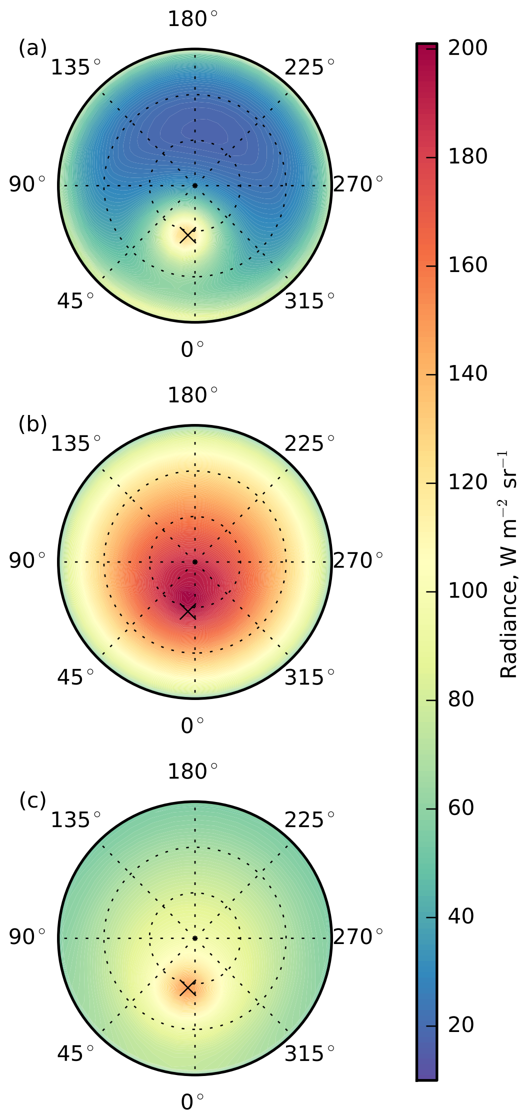

Figure 1: Radiance distributions (looking upwards). Distance from the centre represents polar angle and angular coordinate represents azimuth angle. (a) clear sky radiance distribution, (b) overcast radiance distribution (water cloud optical depth of 8.8), (c) all-sky distribution based on clear sky and cloudy sky distributions with cloud fraction equal to 56.4%. Solar position is represented by X at zenith 32.9°, azimuth 8.2° (the convention in this paper for azimuth is 0° for south, increasing clockwise).

off-zenith. In this example the optical depth of the cloud layer is 8.8, which is thick enough to obscure the solar beam (Oumbe et al., 2008) with the resulting diffuse irradiance approximately isotropically distributed. Fig. 2(c) shows the all-sky tilted irradiance map with the cloud fraction of 56.4%. The optimal tilt of the solar collector is centred around the solar position as in the clear-sky case, but with corresponding lower irradiance values.

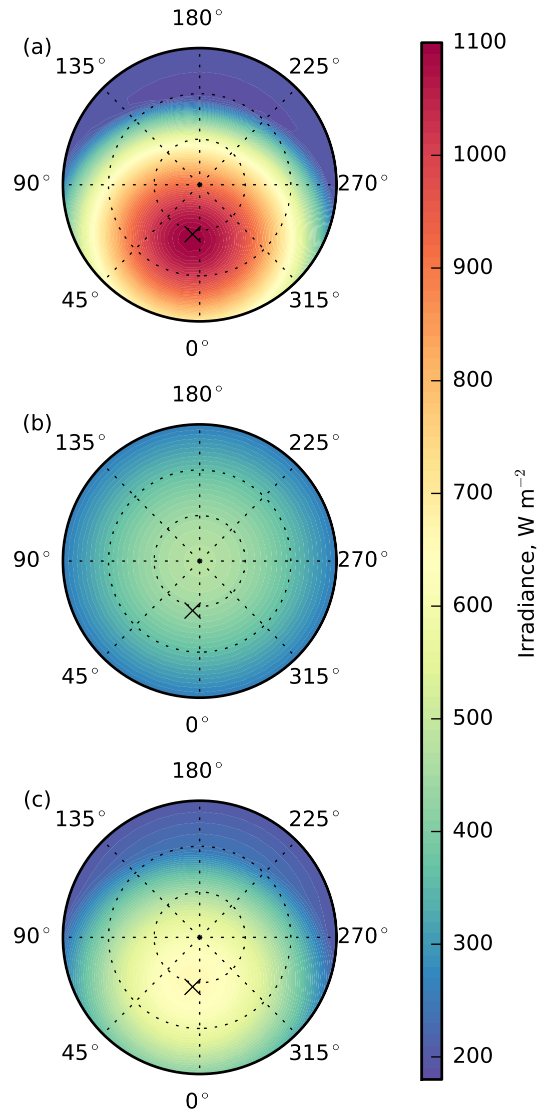

Figure 2: Tilted irradiance maps for the same location as fig. 1. Distance from the centre represents tilt angle with centre representing a horizontal alignment and the edge of the circle represents a vertical alignment. Angular coordinate represents azimuthal alignment. (a) clear sky, (b) overcast sky (water cloud optical depth of 8.8), (c) all-sky with cloud fraction equal to 56.4%. Solar position is represented by X at zenith 32.9°, azimuth 8.2°.

4.3. Yearly tilted irradiation

Radiance distributions were obtained for each hour of the middle day for each 8 day period, and integrated using eq. (4) to produce tilted irradiance. The direct beam contribution was included. Hourly irradiance outputs were then multiplied by the number of days in each period (8, except for the last period of the year which is 5 or 6) and summed to generate the yearly irradiation. For Church Fenton weather station in the UK, the yearly irradiation map is shown in fig. 3.

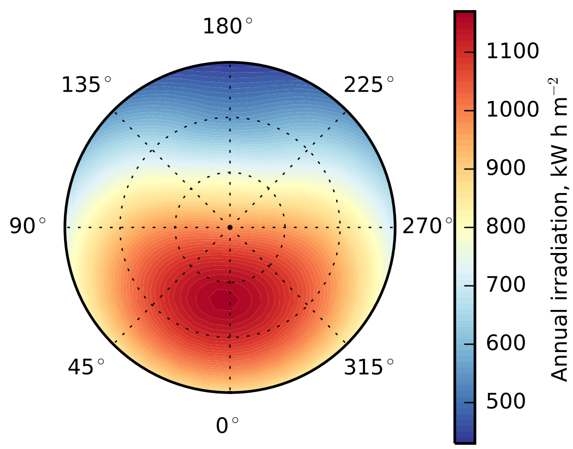

Figure 3: Angled irradiation map for Church Fenton (latitude 53.8°N, longitude 1.2°W, altitude 8 m) for the year of 2013

The optimal south-facing tilt for this location calculated using our method is 40° from the horizontal. The optimal azimuthal alignment here is 6° west of south, highlighting that the afternoon conditions may be clearer than the morning, although the difference in yearly output between 6° and 0° is very small. A "rule of thumb" for annual optimal tilt is that is should be equal to latitude on the basis that this minimises the incidence angle between the solar beam and the normal to the panel surface at solar noon. For areas of the world with significant cloud cover this does not hold true due to the frequent obscuring of the sun by clouds. Christensen and Barker (2001) showed for the US the local clearness index could be used to determine how close to latitude the optimal tilt angle β_{opt} would be with the following relationship:

$$\beta_{\mathrm{opt}} = (0.379 + K_{\mathrm{t,year}})l - 20.6(1 - K_{\mathrm{t,NDJ}}/K_{\mathrm{t,MJJ}}) \tag{8}$$

with l representing latitude and $K_{t,i}$ representing clearness index where for i NDJ = {November, December, January}, MJJ = {May, June, July} and year=annual. For the Church Fenton weather station in fig. 3, $l = 53.8°$, and for 2013 $K_{\mathrm{t,year}} = 0.424$, $K_{\mathrm{t,MJJ}} = 0.458$ and $K_{\mathrm{t,NDJ}} = 0.332$. These low mean clearness indices are indicative of frequently cloudy conditions. Equation (8) predicts $\beta_{\mathrm{opt}} = 38°$ for this station, close to the 40° calculated with the integrated radiance method. Both models suggest the optimal tilt is more horizontal than the angle of latitude at this location.

4.4. Treatment of broken cloud fields

As described in section 3.2, the model uses a linear combination of clear and overcast radiance distributions weighted by the cloud fraction. In reality, clouds exhibit both vertical and horizontal heterogeneity, and our model is a simplification of the 3D picture (Marshak and Davis, 2005). The diffuse reflections from the sides of clouds, along with cloud shadowing, will impact the ground-level radiance field. We therefore compare our radiance distribution to that generated by the UniSky simulator software available from `http://www.unisky.sav.sk` (Kocifaj, 2012; Kocifaj and Fečko, 2014; Kocifaj, 2015). The UniSky simulator can model 3D clouds either as a regular grid, or as randomly orientated. Random clouds can be grouped into a preferred sky sector, simulating the effects of a morning or evening weather front. For random cloud fields, a random seed is specified on input, allowing reproducibility of random simulations.

To keep the simulations consistent, as the two models take different parameters, a simple case is considered. We set the solar zenith angle to be 30° and azimuth to be 0°, cloud fraction 20% with base at 3 km, geometric height 1 km and optical depth 10, and perform a single monochromatic calculation at 550 nm wavelength. A generic aerosol with a Henyey-Greenstein phase function ($g = 0.7$), optical depth $\tau_a = 0.2$ and single scattering albedo $\omega = 0.9$ is prescribed and surface albedo is set to zero. Both models use the nadir-view cloud fraction, which is the proportion of horizontal area covered by clouds to the total area, as viewed from a nadir-viewing instrument such as a satellite.

An additional parameter used in UniSky is the cloud reflectance. This is not supplied explicitly in our model but can be calculated. As cloud reflectance is dependent on optical depth, a plane-parallel cloud with $r_{\text{eff}} = 10$ μm, optical depth 10, base 3 km and vertical extent 1 km, with full Mie phase function, was modelled in libRadtran. Reflectance was found to be 40.7% at 550 nm, based on the ratio of upwelling to downwelling irradiance at the top of atmosphere with molecular scattering and absorption suppressed. Clouds are modelled as spheres in UniSky; the default value of 0.5 km radius is used.

100 runs of the random cloud field in UniSky were generated with the parameters described above, with the random seed ranging sequentially from 1 to 100. Two examples of these diffuse radiance fields for sun unobscured and sun obscured are shown in fig 4. The 100 random runs could simulate a short period of time in which solar zenith angle and weather conditions remain relatively constant overlaid with a wind-driven broken cloud field. As UniSky does not include the DNI as an output (M. Kocifaj, personal communication), this was determined from eq. (5) with the total optical depth the sum of each component:

$$\tau = \tau_c + \tau_a + \tau_R \tag{9}$$

where $\tau_a = 0.2$, τ_R is the Rayleigh scattering optical depth at 550 nm of 0.1014 calculated as in Kocifaj (2012) and τ_c is equal to 10 if the pixel is obscured by cloud and 0 otherwise.

Each of the 100 radiance fields produced by UniSky, along with the calculated beam component, was numerically integrated using a south-facing plane with tilt angle running from 0 to 90°. For the libRadtran run, one radiance field with cloud optical depth of 10 and cloud fraction 0.2 was calculated and the numerical integration applied. The mean value from the 100 UniSky runs is compared to the libRadtran output and the results for tilt angle ranging from 0 to 90° facing south are shown in fig. 5.

In both the libRadtran and the mean of the UniSky runs, the irradiance for this situation is maximised when the tilt angle is 29°. The effect of cloud obscurity can clearly be seen

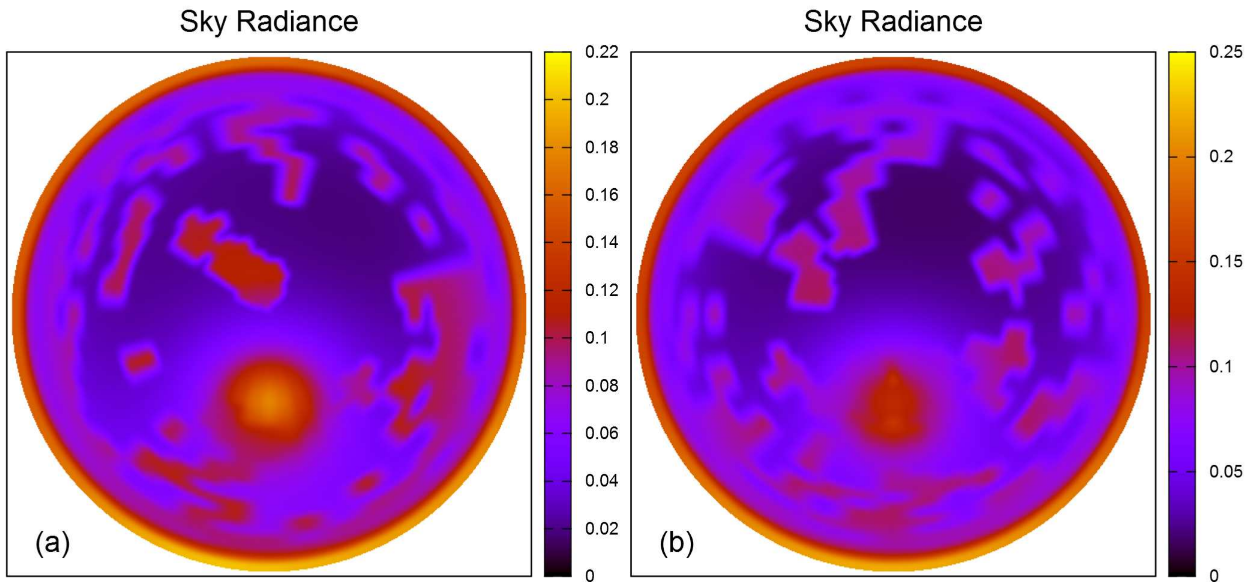

Figure 4: UniSky radiance distributions for two broken cloud regimes ($c_f = 0.2$) where (a) the sun is not obscured and (b) the sun is obscured. Units are radiance normalised to the extraterrestrial DNI [sr^{-1}].

in the bimodal character of the UniSky runs characterised by the clustering of the thin grey lines in fig. 5. When a cloud lies in front of the sun, the irradiance at optimal tilt is around 0.2 of its extraterrestrial values whereas it is close to 0.9 in the unobscured case. The majority of this effect is due to the difference in direct beam transmission between the two modes. The libRadtran method predicts a slightly higher irradiance at all tilt angles under this method compared to UniSky.

As the UniSky simulator does not include multiple scattering within clouds (M. Kocifaj, personal communication), only the gaps between clouds contribute substantially to down-welling radiances. It is recommended (Kocifaj, 2015) to approximate a high cloud fraction with an aerosol layer that represents forward scattering by cloud water droplets. Therefore, for broken clouds under low cloud fraction, the good correspondence between the two models for long-term irradiation totals indicates that the 3D reality can adequately simplified into the 1D weighted clear/overcast simulation, although our model does not replicate an instantaneous scene. For high cloud fractions, the sky diffuse radiances approach the isotropic case, and the 1D approximation used in our model is well-known to be appropriate.

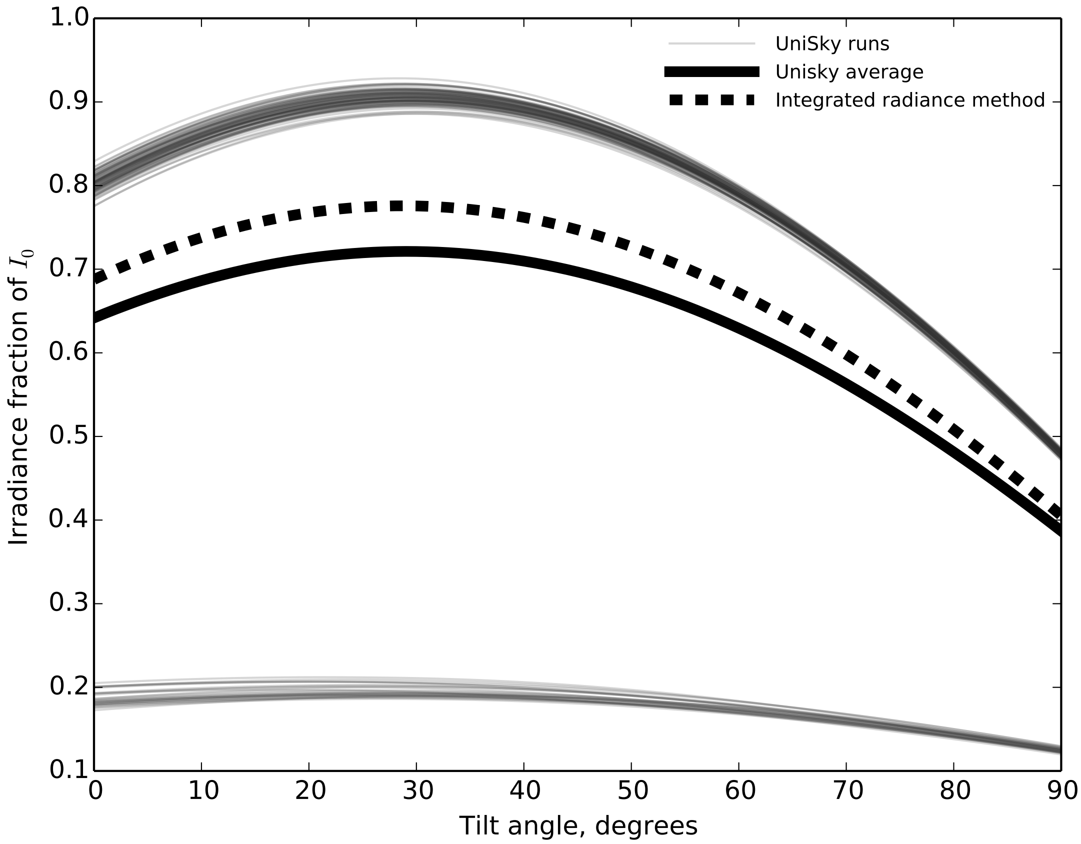

Figure 5: Plane irradiance as a function of panel tilt for 100 runs of the UniSky simulator with random cloud geometry, the UniSky average, and the 1D weighted average radiances from libRadtran, for $\theta_z = 30°$ and $c_f = 0.2$.

4.5. Validation against horizontal irradiation measurements

Yearly irradiation predicted from our model using MODIS data is validated against horizontal irradiation measurements from high-quality pyranometer data and is shown in fig. 6. The UK Met Office MIDAS dataset (Met Office, 2012) is used for UK locations and the Baseline Surface Radiation Network (BSRN) for non-UK locations (BSRN, 2015). The convention in this paper is to use the three-letter BSRN station codes in upper case for BSRN stations and an upper- and lower-case abbreviation for MIDAS stations. Camborne (Cam) and Lerwick (Ler) are MIDAS stations that also supply data to BSRN; at the time of writing the BSRN data were not available so the MIDAS data have been used.

MIDAS provides hourly pyranometer measurements of global horizontal irradiance (GHI) for approximately 100 sites in the UK. The MIDAS data has passed a quality control (QC) procedure run by the UK Met Office. Five MIDAS sites were selected on the basis of wide geographical coverage within the UK and a minimal amount of missing or bad data for 2013. Where missing hours do occur in the MIDAS data, these have been replaced by the mean irradiance from the corresponding hour in the same month.

BSRN provides minutely measurements of horizontal irradiance from sites globally. The BSRN data also contains instances of missing records. Data gaps range from one minute to several days. A QC procedure was applied to the BSRN data to fill in missing or suspect data following the M7 method recommended by Roesch et al. (2011). The M7 method calculates monthly 15-minute means from data where at least 3 minutes per 15-minute period exist and are within the "physically possible" limit for GHI of $1.5S_0 \cos^{1.2}\theta_z + 100$ W m^{-2}. S_0 is the solar constant I_0 corrected for earth-sun distance. The monthly mean is only valid if all 96 15-minute bins contain valid values. Only sites where all months of 2013 data were available and passed the QC check were selected for the BSRN validation. The details of the 27 meteorological stations used in the validation are shown in the appendix. Solar irradiance at BSRN sites is measured with a Kipp & Zonen CMP21 or CMP22 pyranometer with the exception of Tamanrasset which uses the Eppley PSP, all of which are World Meteorological Organisation (WMO) High Quality certified.

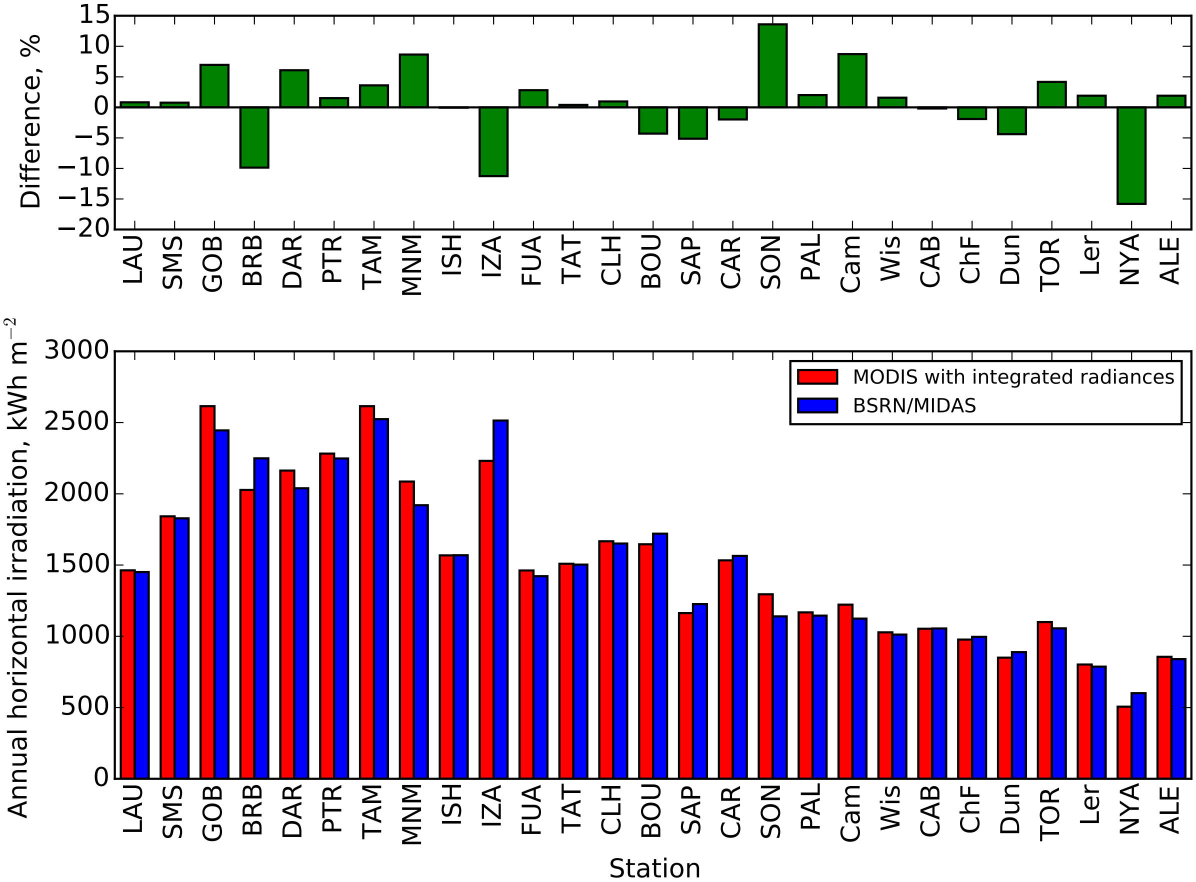

Figure 6: Validation of integrated radiance method using MODIS data against pyranometer measurements. For station names and locations please refer to Appendix.

The mean bias difference (MBD) between the annual irradiation derived from our method and the pyranometer data is +0.56% and the root-mean-square difference (RMSD) is +6.69%. Of the sites where our method deviates from the measured values by more than 10%, two (IZA and SON) are at mountaintop sites at altitudes 2373 m and 3109 m respectively. In these areas, the 1° resolution of the MODIS atmosphere data may not be large enough to capture all of the micro-climatic effects in mountainous regions. As discussed by Gueymard and Wilcox (2011), the spatial variation in irradiance measurements is highest in coastal and mountainous areas. Clouds are particularly difficult to attribute as sometimes the site location may be above the mean cloud height for the 8 day period whereas in reality the station is not cloud-free for the entire 8 days. Furthermore if the cloud deck is below the station altitude, the albedo from the point of view of the pyranometer changes, and backscattering effects between the cloud layer and the atmosphere above the station can enhance the downwards radiation. It is unlikely that the MODIS albedo product includes these effects as it is calculated from clear sky scenes.

The other location with a greater than 10% absolute error, NYA, is at very high latitude (78.9°N), where satellite retrievals from MODIS become less reliable. In addition, in such a high-latitude site, solar declination can vary widely over the course of an 8-day period in spring and autumn and as such the solar geometry used in our calculations may not be representative. Interestingly, the other high latitude location, ALE in the far north of Canada (82.5°N), shows a very good agreement with the model. This could be due to a higher annual irradiation than NYA indicative of clearer conditions as the annual horizontal irradiation at ALE is similar to that at Dun at 56.4°N. BRB, the fourth poorest site for agreement with a 9.9% underestimation, suffers from a large amount of incomplete data in the 2013 BSRN dataset which may result in a large error in the “measurement” value for this site. BRB passes the QC test because all 96 15-minute bins are present for each month, but for some months there are as little as 7 days of data present.

4.6. Results of the tilted irradiation and comparison with PVGIS

It is difficult to validate the tilted irradiation model on a global basis because there are few comparable high-quality long term measurements of tilted irradiance available worldwide. In section 4.7 we validate our results against data from one site. The optimal tilt angle predicted by the integrated radiance model, and the irradiance predicted at this optimal tilt, are compared with results from the online PVGIS solar resource estimation tool in fig. 7 (European Commission, 2012). PVGIS is a validated model that derives solar irradiance from the Meteosat satellite cloud product and calculates tilted irradiance using the Muneer model (Muneer, 1990). Additionally the PVGIS model reports GHI with a mean bias error (MBE) of within ±5% for all but 4 BSRN and other surface irradiance measurement sites out of 23 (Huld et al., 2012) whereas the Muneer (1990) tilt model gives a MBE of +5.3% and root-mean-squared error (RMSE) of 9.6% for vertical, south-facing planes, with considerably lower errors for 45° and 60° south-facing planes for the EU Joint Research Centre (JRC) test site at Ispra, Italy. 13 of the 27 validation sites used in section 4.5 fall within the spatial boundaries of PVGIS and have been compared in fig. 7.

The comparisons do not correspond to the same time period as the PVGIS database uses data from the CM-SAF satellite products, namely Meteosat First Generation (MFG, 1998–2005) and Meteosat Second Generation (MSG, 2006–2011), and it is not stated which particular BSRN station years are used to validate these datasets (Huld et al., 2012). Our validation against BSRN and MIDAS ground stations uses 2013 data. The comparison with PVGIS is not a validation of our model for this reason, but a sense-check against a widely-used tilted irradiance database. Nevertheless some systematic differences can be observed. The top panel of fig. 7 shows that in the majority of locations our predicted annual optimal tilt angle is steeper than in PVGIS, ranging from $-1°$ at CAR and Cam to $+8°$ at TOR. Part of the differences may be due to, on average, higher GHI values predicted from our model compared to PVGIS, suggesting that our model predicts a lower cloud fraction or greater cloud transmission than PVGIS does in general. The effect of this is large at the three low latitude sites of GOB, TAM and IZA where in each case our model predicts an optimal tilt slightly steeper than the latitude location, showing the influence of the direct beam and circumsolar diffuse components of solar radiation. For IZA it is interesting to note that our model under-predicts GHI for the 2013 calendar year quite substantially compared to the BSRN pyranometer data, whereas the PVGIS estimate is even lower (although not validated against the same time period as previously mentioned). This, along with results for SON reported by Huld et al. (2012) and our data shown in fig. 6, shows the difficulties that both models experience in mountainous areas.

The middle and bottom panels of fig. 7 shows that in every location there is a more positive difference in the irradiation at optimal tilt than the GHI between our model and PVGIS. This effect is seen even at CAR and Cam indicating a difference between the Muneer tilt model used in PVGIS and the integrated radiance method. This is emphasised by the

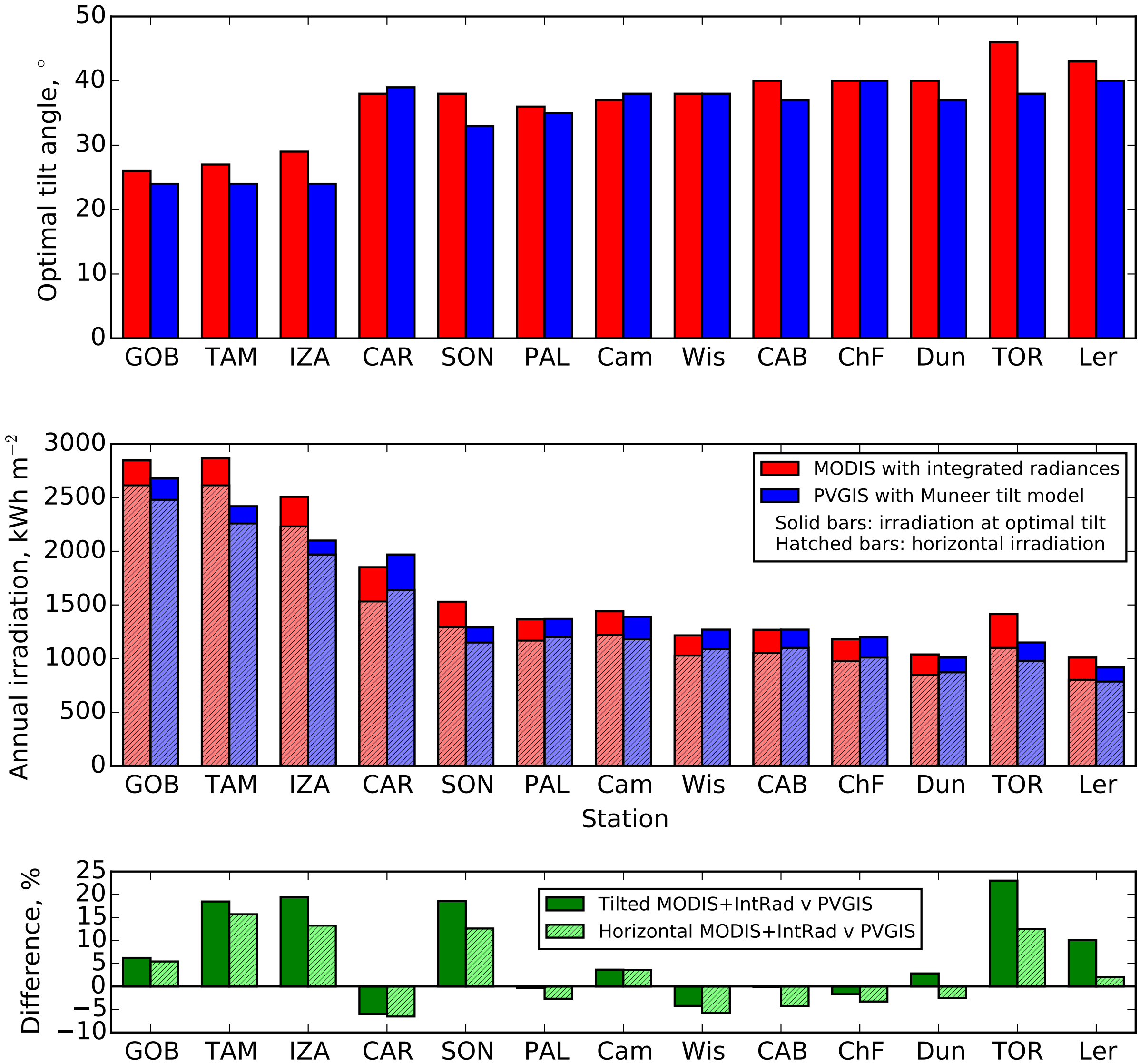

Figure 7: Comparison of integrated radiance method using MODIS data against results from PVGIS for optimal tilt angle and yearly irradiation at optimal tilt. The top figure compares optimal tilt angles between the two models, the middle figure shows irradiation at optimal tilt (solid bars) and GHI (pale hatched bars), and the bottom figure shows the differences between the two models for irradiation at optimal tilt (solid bars) and for GHI (pale hatched bars). For station names and locations please refer to table 2 in the Appendix.

Dun site where PVGIS predicts a higher annual GHI total but lower irradiation at optimal tilt.

Tilt	Integrated radiance model (kWh m^{-2} yr^{-1})	Eppley PSP measurements (kWh m^{-2} yr^{-1})	Difference
Horizontal	1760.0	1684.2	+4.5%
40°S	2120.4	2010.0	+5.5%
90°S	1479.3	1402.9	+5.4%
90°E	1085.4	1138.6	−4.7%
90°W	976.7	922.2	+5.9%
90°N	420.5	479.3	−12.3%

Table 1: Validation of tilted irradiation from the integrated radiance model against ground measurements from NREL.

4.7. Validation against tilted irradiation measurements from the National Renewable Energy Laboratory Baseline Measurement System

The NREL Solar Radiation Research Laboratoty (SRRL) (Andreas and Stoffel, 1981) produces horizontal and tilted irradiation datasets which are available from their website at `http://www.nrel.gov/midc/srrl_bms/`. Tilted irradiation is measured at 40°S and at 90°S, W, E and N, using Eppley PSP pyranometers. Horizontal radiation is measured with a number of different pyranometer models. For consistency, we use the ventilated, corrected Eppley PSP horizontal irradiation measurement. The NREL site is located in Golden, Colorado, at 39.74°N, 105.18°W at an altitude of 1829 m.

The validation against the NREL station measurements is shown in table 1. The horizontal irradiation estimate from the integrated radiance model is 4.5% higher than the NREL measurement using the Eppley PSP. For the 40° and 90° south-facing tilts, the relative error is slightly higher but does not grow appreciably. The model captures some of the diurnal variation in weather conditions at this site, as seen by the differences between east- and west-facing tilt estimates, however underestimates the magnitude of the diurnal variation with an overestimate for the west-facing pyranometer and an underestimate for the east-facing pyranometer. This may be due to the timing of the satellite overpasses, approximately 90 minutes before and after local solar noon on average, whereas east- and west-facing wall irradiances will be at their maximum earlier and later in the day, respectively. The north-facing estimate is considerably less good than for the other orientations, however, it is not likely that serious consideration would be given to tilting panels poleward given the low overall yield estimate.

5. Discussion

The integrated radiance method is possible to evaluate globally as the satellite retrieval data from MODIS has global coverage. The method is applicable to any dataset in which aerosol parameters, ozone, water vapour, cloud liquid water path, cloud ice water path and cloud fraction are available. The necessary inputs to the model also exist in meteorological reanalysis and climate models. The aerosol parameters are available in MODIS but often suffer from large gaps in data, so in our model they are obtained from the GLOMAP global aerosol model. Aerosol reanalysis datasets such as MACC (`http://apps.ecmwf.int/datasets/data/macc-reanalysis`), which assimilates observations and forecasts into a consistent gridded dataset, can be used. Thus, the integrated radiance model can be used for determining a realistic optimal tilt for an arbitrary climatic condition, and solar energy resource calculated on this basis.

It should be mentioned that MODIS satellite retrievals are not always available or are of low quality. The limit of MODIS orbital tracks are at 82° N/S, and for latitudes greater than 77° N/S the satellite tracks overlap. Successive retrievals may not be independent and observational nadir angles may be higher towards the poles as the satellites do not overpass above/below 82° N/S (Hubanks et al., 2008). On the other hand, these regions are currently unimportant for solar energy generation. A more critical issue occurs when albedo values are not reported over a 16-day period. As an albedo retrieval requires a cloudless scene when the satellite overpasses, it is possible that there are no clear overpasses during a 16-day period for some parts of the world. In these cases where no albedo measurement exists for a $0.05° \times 0.05°$ cell, the mean value from the 21×21 cells surrounding the grid square ($1.05° \times 1.05°$) is used. In very rare cases where no 1.05° mean exists, the spectral albedo is taken from the global $0.17° \times 0.17°$ map of 20 different surface types in the IGBP land cover dataset (Belward and Loveland, 1996).

In many regions, clouds are the largest input uncertainty in our model because the radiative properties of aerosols, water vapour and ozone are less significant when the entire solar spectrum is considered. The direct and diffuse radiation fields are spectrally dependent (Forster and Shine, 1995) and although a spectral calculation is performed and then integrated over all solar wavelengths to obtain broadband irradiance, the spectrally-dependent irradiance was not considered. When applied to assessing the energy output of PV technologies, spectral considerations have shown to be important and this could affect the optimal PV tilt angle.

It is possible to improve the spatial and temporal resolution of the results obtained. MODIS Level 3 8-day mean data has been used in this model for atmosphere and albedo. Level 3 data is available daily, the use of which may improve accuracy at the expense of an 8-fold increase in computational time. Greater accuracy may be obtained by using the Level 2 satellite swath data, which has a nadir resolution of 1 km and will usually overpass a location at least once per day, although there are small gaps in the satellite overpass tracks near the equator that are not covered every day by the Level 2 or Level 3 daily data. To use higher resolution data will require many more RT simulations per location per year, and will need the use of pre-calculated lookup tables or a polynomial regression fit to allow swifter calculation of the radiance fields. This is an area for future investigation. It is shown however that for locations at low and moderate altitude and latitude, sufficient agreement for horizontal and equator-facing tilts for yearly irradiation is obtained with the 8-day data.

6. Conclusion

This paper presents a computational method to calculate the all-sky irradiance on a plane of arbitrary alignment, which is globally applicable. The optimal tilt angle at a particular location is dependent on the meteorological conditions and cannot be related to a single parameter. A radiative transfer simulation is run to produce a ground-level radiance field, which is numerically integrated over the tilt angle of interest. The required inputs of cloud liquid water path, cloud ice water path, cloud fraction, temperature, ozone, water vapour and surface albedo are standard variables from satellite observations, meteorological reanalysis or climate model data. We use MODIS Terra and Aqua satellite data for clouds, ozone, water vapour and albedo. Aerosols are provided by the GLOMAP model but any scheme that provides the aerosol phase function, optical depth and single scattering albedo can be used. The horizontal irradiation predicted by our model is compared to contemporaneous pyranometer data from MIDAS and BSRN and agrees to within ±10% for all but 3 sites out of 27. The MBD between our method and BSRN/MIDAS across all sites is +0.56% and RMSD is 6.69% for horizontal irradiance.

When validated against the NREL tilted irradiance dataset our model predicts the annual irradiation within ±6% for all orientations except 90°N. The magnitude of error for tilted irradiance on 40° and 90° south-facing planes is similar to that for horizontal irradiance. The diurnal variation in prevaling weather conditions is partially captured by analysis of the difference between east- and west-facing estimates of annual irradiation compared to pyranomter measurements, although underestimated. Due to a lack of high-quality tilted irradiance measurement stations, it is not possible to validate against tilted irradiance measurements globally, but the validated PVGIS model is used as a comparison. The main differences between our model and the Muneer (1990) tilt model used in PVGIS are the steeper optimal tilt angles and more positive relative differences between tilted irradiation and horizontal irradiation. In mid-latitude and low-to-moderate altitude sites, where PVGIS has been validated, the models produce similar results. In order to draw more robust conclusions about the optimal tilt angle from the model, a larger network of tilted irradiance measurements would be required. However, the limited model comparisons and validations show that the model produces sensible results and could be applied where ground measurements of tilted irradiance are not available. Further work in this area includes accounting for horizon shading, and producing a global map of optimal annual tilt.

Acknowledgements

The authors would like to thank Arve Kylling of the Norwegian Institute for Air Research for assistance with interpreting the radiance output from libRadtran and its application to tilted planes, Miroslav Kocifaj (Slovak Academy of Sciences) for detailed discussions in relation to the UniSky simulator tool, and Catherine Scott for provision of the GLOMAP aerosol dataset. The work of the BSRN station managers in providing the surface radiation dataset is acknowledged, as is the work of the NREL staff that provide the irradiance measurements for the NREL Baseline Measurement System. We are grateful to the UK Met Office for providing the MIDAS irradiance data through the British Atmospheric Data Centre. The MODIS data used in this study were acquired as part of the NASA's Earth-Sun System Division and archived and distributed by the MODIS Adaptive Processing System (MODAPS), acquired from the Level 1 and Atmosphere Archive and Distribution System (LAADS). This work was financially supported by the Engineering and Physical Sciences Research Council through the University of Leeds Doctoral Training Centre in Low Carbon Technologies (grant number EP/G036608/1).

Appendix

Code	Station name	Country	Lat.	Lon.	Alt. (m)	Network
LAU	Lauder	New Zealand	45.045°S	169.689°E	350	BSRN
SMS	São Martinho	Brazil	29.443°S	53.823°W	489	BSRN
GOB	Gobabeb	Namibia	23.561°S	15.042°E	407	BSRN
BRB	Brasilia	Brazil	15.601°S	47.713°W	1023	BSRN
DAR	Darwin	Australia	12.420°S	130.891°E	350	BSRN
PTR	Petrolina	Brazil	9.068°S	40.319°W	387	BSRN
TAM	Tamanrasset	Algeria	22.780°N	5.510°E	1366	BSRN
MNM	Minamitorishima	Japan	24.288°N	153.983°E	7	BSRN
ISH	Ishigakijima	Japan	24.337°N	124.163°E	6	BSRN
IZA	Izaña	Tenerife	28.309°N	16.499°W	2373	BSRN
FUA	Fukuoka	Japan	33.582°N	130.375°E	3	BSRN
TAT	Tateno	Japan	36.050°N	140.133°E	25	BSRN
CLH	Chesapeake Light	USA	36.905°N	75.713°W	37	BSRN
BOU	Boulder	USA	40.050°N	105.007°W	1577	BSRN
SAP	Sapporo	Japan	43.060°N	141.329°E	17	BSRN
CAR	Carpentras	France	44.083°N	5.059°E	100	BSRN
SON	Sonnblick	Austria	47.054°N	12.958°E	3109	BSRN
PAL	Palaiseau	France	48.713°N	2.208°E	156	BSRN
Cam	Camborne	UK	50.218°N	5.327°W	87	MIDAS
Wis	Wisley	UK	51.310°N	0.475°W	38	MIDAS
CAB	Cabauw	Netherlands	51.971°N	4.927°E	0	BSRN
ChF	Church Fenton	UK	53.836°N	1.197°W	8	MIDAS
Dun	Dunstaffnage	UK	56.451°N	5.439°W	3	MIDAS
TOR	Toravere	Estonia	58.254°N	26.462°E	70	BSRN
Ler	Lerwick	UK	60.140°N	1.183°W	82	MIDAS
NYA	Ny-Ålesund	Svalbard	78.925°N	11.930°E	11	BSRN
ALE	Alert	Canada	82.490°N	62.420°W	127	BSRN

Table 2: List of BSRN and UKMO-MIDAS stations used in the validation and comparison.

References

Anderson, G., Clough, S., Kneizys, F., Chetwynd, J., Shettle, E., 1986. AFGL Atmospheric Constituent Profiles (0–120km). Air Force Geophysics Laboratory.

Andreas, A., Stoffel, T., 1981. NREL Solar Radiation Research Laboratory (SRRL): Baseline Measurement System (BMS). Tech. Rep. DA-5500-56488, Golden, Colorado, `http://dx.doi.org/10.5439/1052221`.

Baum, B., Heymsfield, A., Yang, P., Bedka, S., 2005. Bulk scattering properties for the remote sensing of ice clouds. Part I: Microphysical data and models. Journal of Applied Meteorology 44, 1885–1895.

Baum, B., Yang, P., Heymsfield, A., Bansemer, A., Cole, B., Merrelli, A., Wang, C., 2014. Ice cloud single-scattering property models with the full phase matrix at wavelengths from 0.2 to 100 μm. Journal of Quantitative Spectroscopy & Radiative Transfer 146, 123–139.

Behrendt, T., Kuehnert, J., Hammer, A., Lorenz, E., Betcke, J., Heinemann, D., 2013. Solar spectral irradiance derived from satellite data: A tool to improve thin film PV performance estimations? Solar Energy 98, 100–110.

Belward, A., Loveland, T., 1996. The DIS 1-km land cover data set. Global Change, the IGBP Newsletter 27.

Bird, R., Riordan, C., 1986. Simple solar spectral model for direct and diffuse irradiance on horizontal and tilted planes at the earth's surface for cloudless atmospheres. Journal of Climate and Applied Meteorology 25 (1), 87–97.

Blanc, P., Espinar, B., Geuder, N., Gueymard, C., Meyer, R., Pitz-Paal, R., Reinhardt, B., Renné, D., Sengupta, M., Wald, L., Wilbert, S., 2014. Direct normal irradiance related definitions and applications: The circumsolar issue. Solar Energy 110, 561–577.

Brunger, A., Hooper, F., 1993. Anisotropic sky radiance model based on narrow field of view measurements of shortwave radiance. Solar Energy 51 (1), 53–64.

BSRN, 2015. World Radiation Monitoring Center – Baseline Surface Radiation Network. http://bsrn.awi.de/, accessed 10.07.2015.

Bugler, J., 1977. The determination of hourly insolation on an inclined plane using a diffuse irradiance model based on hourly measured global horizontal insolation. Solar Energy 19 (6), 477–491.

Cano, D., Monget, J., Albuisson, M., Guillard, H., Regas, N., Wald, L., 1986. A method for the determination of the global solar radiation from meteorological satellite data. Solar Energy 37 (1), 31–39.

Christensen, C., Barker, G., 21–25 April 2001. Effects of tilt and azimuth on annual incident solar radiation for United States locations. In: Solar Forum. Washington DC, USA.

Dahlback, A., Stamnes, K., 1991. A new spherical model for computing the radiation field available for photolysis and heating at twilight. Planetary and Space Science 39 (5), 671–683.

Deneke, H., Feijt, A., Roebeling, R., 2008. Estimating surface solar irradiance from METEOSAT SEVIRI-derived cloud properties. Remote Sensing of Environment 112, 3131–3141.

European Commission, 2012. Photovoltaic Geographical Information System (PVGIS). http://re.jrc.ec.europa.eu/pvgis/index.htm, accessed 26.09.2014.

Forster, P., Shine, K., 1995. A comparison of two radiation schemes for calculating ultraviolet radiation. Quarterly Journal of the Royal Meteorological Society 121, 1113–1131.

Gracia-Amillo, A., Huld, T., 2013. Performance comparison of different models for the estimation of global irradiance on inclined surfaces. European Commission, Joint Research Centre, Via Enrico Fermi 2749, TP 450, 21027 Ispra (VA), Italy.

Gueymard, C., 1987. An anisotropic solar irradiance model for tilted surfaces and its comparison with selected engineering algorithms. Solar Energy 38 (5), 367–386.

Gueymard, C., 1995. SMARTS2, A simple model of the atmospheric radiative transfer of sunshine: algorithms and performance assessment. Florida Solar Energy Center.

Gueymard, C., 2009. Direct and indirect uncertainties in the prediction of tilted irradiance for solar engineering applications. Solar Energy 83, 432–444.

Gueymard, C., Wilcox, S., 2011. Assessment of spatial and temporal variability in the US solar resource from radiometric measurement and predictions from models using ground-based or satellite data. Solar Energy 85 (5), 1068–1084.

Hay, J., Davies, J., 1980. Calculation of the solar radiation incident on an inclined surface. In: Hay, J., Won, T. (Eds.), Proceedings First Canadian Solar Radiation Data Workshop. Atmospheric Environment Service, Toronto, pp. 59–72.

Hu, Y., Stamnes, K., 1993. An accurate parameterization of the radiative properties of water clouds suitable for use in climate models. Journal of Climate 6, 728–742.

Hubanks, P., King, M., Platnick, S., Pincus, R., 2008. MODIS atmosphere L3 gridded product algorithm theoretical basis document.

Huld, T., Müller, R., Gambardella, A., 2012. A new solar radiation database for estimating PV performance in Europe and Africa. Solar Energy 86, 1803–1815.

Kato, S., Ackerman, T. P., Mather, J. H., Clothiaux, E. E., 1999. The k-distribution method and correlated-k approximation for a shortwave radiative transfer model. Journal of Quantitative Spectroscopy & Radiative Transfer 62, 109–121.

Key, J., Yang, P., Baum, B., Nasiri, S., 2002. Parameterization of shortwave ice cloud optical properties for various particle habits. Journal of Geophysical Research: Atmospheres 107 (D13), AAC 7–1–AAC 7–10.

Klucher, T., 1979. Evaluation of models to predict insolation on tilted surfaces. Solar Energy 23, 111–114.

Kocifaj, M., 2012. Angular distribution of scattered radiation under broken cloud arrays: An approximation of successive orders of scattering. Solar Energy 86, 3575–3586.

Kocifaj, M., 2015. Unified model of radiance patterns under arbitrary sky conditions. Solar Energy 115, 40–51.

Kocifaj, M., Fečko, S., 2014. Unisky simulator. http://www.unisky.sav.sk.

Lohmann, S., Schillings, C., Mayer, B., Meyer, R., 2006. Long-term variability of solar direct and global radiation derived from ISCCP data and comparison with reanalysis data. Solar Energy 80, 1390–1401.

Marshak, A., Davis, A. (Eds.), 2005. 3D Radiative Transfer in Cloudy Atmospheres. Springer.

Mayer, B., Kylling, A., 2005. Technical note: The libRadtran software package for radiative transfer calculations – description and examples of use. Atmospheric Chemistry and Physics 5, 1855–1877.

Mayer, B., Kylling, A., Emde, C., Hamann, U., Buras, R., 2012. libRadtran user's guide. http://www.libradtran.org.

McArthur, L., Hay, J., 1981. A technique for mapping the distribution of diffuse solar radiation over the sky hemisphere. Journal of Applied Meteorology 20 (4), 421–429.

Menzel, W., Frey, R., Baum, B., 2010. Cloud top properties and cloud phase algorithm theoretical basis document. http://modis-atmos.gsfc.nasa.gov/_docs/CTP_ATBD_oct10.pdf.

Met Office, 2012. Met Office Integrated Data Archive System (MIDAS) land and marine surface stations data (1853-current). http://catalogue.ceda.ac.uk/uuid/220a65615218d5c9cc9e4785a3234bd0, accessed 10.07.2015.

Minnis, P., Sun-Mack, S., Young, D., Heck, P., Garber, D., Chen, Y., Spangenberg, D., Arduini, R., Trepte, Q., Smith, W., Ayers, J., Gibson, S., Miller, W., Hong, G., Chakrapani, V., Takano, Y., Liou, K.-N., Xie, Y., Yang, P., 2011. CERES Edition-2 cloud property retrievals using TRMM VIRS and Terra and Aqua MODIS data—part I: Algorithms. IEEE Transactions on Geoscience and Remote Sensing 49 (11), 4374–4400.

Mueller, R., Dagestad, K., Ineichen, P., Schroedter-Homscheidt, M., Cros, S., Dumortier, D., Kuhlemann, R., Olseth, J., Pieravieja, G., Reise, C., Wald, L., Heinemann, D., 2004. Rethinking satellite-based solar irradiance modelling: The SOLIS clear-sky module. Remote Sensing of Environment 91, 160–174.

Mueller, R., Matsoukas, C., Gratzki, A., Behr, H., Hollman, R., 2009. The CM-SAF operational scheme for the satellite based retrieval of solar surface irradiance – a LUT based eigenvector hybrid approach. Remote Sensing of Environment 113, 1012–1024.

Muneer, T., 1990. Solar radiation model for Europe. Building Services Engineering Research and Technology 11 (4), 153–163.

Nann, S., Emery, K., 1992. Spectral effects on PV-device rating. Solar Energy Materials and Solar Cells 27, 189–216.

Oumbe, A., Wald, L., Blanc, P., Schroedter-Homscheidt, M., 7–10 October 2008. Exploitation of radiative transfer model for assessing solar resource radiation: the relative importance of atmospheric constituents. In: EUROSUN2008, 1st International Congress on Heating, Cooling and Buildings. Lisbon, Portugal.

Perez, R., Ineichen, P., Seals, R., Michalsky, J., Stewart, R., 1990. Modeling daylight availability and irradiance components from direct and global irradiance. Solar Energy 44 (5), 271–189.

Reindl, D., Beckman, W., Duffie, J., 1990. Evaluation of hourly tilted surface radiation models. Solar Energy 45, 9–17.

Roesch, A., Wild, M., Ohmura, A., Dutton, E., Long, C., Zhang, T., 2011. Assessment of BSRN radiation records for the computation of monthly means. Atmospheric Measurement Techniques 4 (2), 339–354.

Rozwadowska, A., 2004. Optical thickness of stratiform clouds over the Baltic inferred from on-board irradiance measurements. Atmospheric Research 72, 129–147.

Scott, C. E., Rap, A., Spracklen, D. V., Forster, P. M., Carslaw, K. S., Mann, G. W., Pringle, K. J., Kivekäs, N., Kulmala, M., Lihavainen, H., Tunved, P., 2014. The direct and indirect radiative effects of biogenic secondary organic aerosol. Atmospheric Chemistry and Physics 14 (1), 447–470.

Skartveit, A., Olseth, J., 1986. Modelling slope irradiance at high latitudes. Solar Energy 36 (4), 333–344.

Stamnes, K., Tsay, S.-C., Wiscombe, W., Laszlo, I., 2000. DISORT, a General-Purpose Fortran Program for Discrete-Ordinate-Method Radiative Transfer in Scattering and Emitting Layered Media: Documentation of Methodology. Dept. of Physics and Engineering Physics, Stevens Institute of Technology, Hoboken, NJ, USA.

Willmott, C., 1982. On the climatic optimization of the tilt and azimuth of flat-plate solar collectors. Solar Energy 28, 205–216.

Wiscombe, W., 1980. Improved Mie scattering algorithms. Applied Optics 19 (9), 1505–1509.

Xie, Y., Yang, P., Gao, B.-C., Kattawar, G., Mishchenko, M., 2006. Effect of ice crystal shape and effective size on snow bidirectional reflectance. Journal of Quantitative Spectroscopy and Radiative Transfer 100 (1–3), 457–469.

Xie, Y., Yang, P., Kattawar, G., Minnis, P., Hu, Y., Wu, D., 2012. Determination of ice cloud models using MODIS and MISR data. International Journal of Remote Sensing 33 (13), 4219–4253.